RSC Advances

PAPER

Cite this: *RSC Adv.*, 2024, **14**, 11456

The effect of the gelation temperature on the structural, magnetic and magnetocaloric properties of perovskite nanoparticles manufactured using the sol–gel method

Line Karoui, *[a] Mourad Smari [b] and Taoufik Mnasri[a]

This study presents a comprehensive investigation of the structural and magnetic properties of $La_{0.8}Sr_{0.2}Mn_{0.8}Co_{0.2}O_3$ (LS1, LS2 and LS3) compounds synthesized *via* the sol–gel method at different gelation temperatures through X-ray diffraction and different magnetic measurement techniques. The Rietveld refinement demonstrated that all samples exhibit a rhombohedral perovskite structure with the $R\bar{3}C$ space group. Their magnetic behavior, characterized through magnetization measurements, hysteresis loops, and Arrot plots, demonstrates a ferromagnetic–paramagnetic transition with notable soft ferromagnetic characteristics. The samples also demonstrate second-order magnetic transitions, short-range magnetic order and the presence of both ferromagnetic and antiferromagnetic contributions. AC magnetic susceptibility measurements, allowing the investigation of the magnetic dynamics of the samples, shows that the Vogel–Fulcher and the Conventional Critical Slowing Down models are the most appropriate for describing the dynamic behavior, confirming the spin-glass nature of the compounds and the presence of medium to strong interaction between magnetic nanoparticles. The influence of gelation temperature in the magnetocaloric effect of the compounds was proven and LS1, synthesized at the lowest gelation temperature (70 °C), exhibits the higher magnetic entropy change ($|\Delta S_{max}| = 3.25$ J kg^{-1} K^{-1} and RCP = 209.83 J kg^{-1} at 5 T). For a better evaluation of the magnetocaloric efficiency, the temperature average entropy change (TEC) parameter was calculated for all three samples and LS1 showed the highest value (TEC (LS1) ~3.2 J kg^{-1} K^{-1} for $\Delta T_{H-C} = 10$ K and $\Delta H = 5$ T).

Received 12th February 2024
Accepted 3rd April 2024

DOI: 10.1039/d4ra01086h

rsc.li/rsc-advances

1 Introduction

Perovskite materials have garnered significant recognition in various fields of physics and industrial technology due to their unique crystal structure and versatile properties.[1–4] In the realm of materials science, the family of oxide perovskite compounds, characterized by the general formula $R_{1-x}A_xMnO_3$, has emerged as an intriguing research area. Among these compounds, $La_{1-x}Sr_xMnO_3$ (LSMO) stands out as a promising candidate for a wide range of technological applications, including solid oxide fuel cells, refrigeration, magnetic sensors, and catalysis.[5–7]

One of the key factors that contributes to the diverse properties of LSMO is the substitution of strontium (Sr) for lanthanum (La) at the A-site of the crystal structure. This substitution induces a distortion in the crystalline lattice, resulting in a variation in the Mn–O–Mn bond angle. This structural transformation plays a crucial role in converting the material from its initial antiferromagnetic state, observed in the parent compound $LaMnO_3$, to a new ferromagnetic compound when a rhombohedral distortion is present.[8] The ability to manipulate the magnetic behavior through structural modification makes LSMO compound attractive for numerous applications.

LSMO also exhibits intriguing phenomena within a specific temperature range centered around the Curie temperature. Two notable phenomena are the magnetocaloric effect and the giant magnetoresistance,[6,9] which have significant implications for cooling and sensor technologies.

To further enhance the performance of LSMO and tailor its properties for specific applications, the introduction of transition metal dopants, such as cobalt (Co), has been investigated. The incorporation of Co into the crystal structure alters the magnetic interactions between Mn^{3+} and Mn^{4+} ions, favoring antiferromagnetic super-exchange interactions over ferromagnetic double–exchange interactions. This doping-induced modification leads the emergence of inhomogeneities within the material, resulting in short-range magnetic order, a decrease in the Curie temperature,[10] an increased variation of magnetic entropy, and the possible existence of spin-glass or superparamagnetic states.[11,12]

[a]*Laboratory of Technology, Energy and Innovative Materials, TEMI, Department of Physics, Faculty of Sciences of Gafsa, University of Gafsa, 2112, Tunisia. E-mail: linekaroui5@gmail.com*

[b]*Applied Physics Laboratory, Faculty of Sciences of Sfax, University of Sfax, B.P. 1171, 3000 Sfax, Tunisia*

While previous studies have primarily focused on investigating the effect of different substitution ratios of cobalt at the Mn site and various synthesis methods on the physical properties of $La_{1-x}Sr_xMn_{1-y}Co_yO_3$ compounds,[13,14] this study aims to explore the influence of gelation temperature on physical properties of $La_{0.8}Sr_{0.2}Mn_{0.8}Co_{0.2}O_3$ during the preparation process using the sol–gel technique. The incorporation of Co at such a doping concentration (0.2) optimizes the magnetoresistance and simultaneously eliminates its temperature dependence.[15] Furthermore, 0.2 is approximately the critical doping concentration of cobalt in $La_{0.8}Sr_{0.2}MnO_3$, as evidenced by the typical insulator characteristics observed in the low temperature transport property when the doping concentration reaches 0.3.[15,16]

The sol–gel synthesis method offers precise control over the composition and structure of the resulting material. Specifically, we examine the structural and magnetic properties of $La_{0.8}Sr_{0.2}Mn_{0.8}Co_{0.2}O_3$ samples prepared at different gelation temperatures. By systematically varying the gelation temperature, we can investigate its impact on the properties of the samples and understand how this parameter affects the crystalline structure, the cooling performance and the magnetic behavior of the synthesized samples.

2 Experimental

The samples denoted as LS1, LS2 and LS3 with a chemical formula $La_{0.8}Sr_{0.2}Mn_{0.8}Co_{0.2}O_3$, were synthesized utilizing the sol–gel approach and precise amounts of all precursors, a clear red solution was acquired, which was then heated to form a resin. The gelation temperature of the samples was set at 70 °C for LS1, 90 °C for LS2 and 300 °C for LS3. To produce ashes, the samples were heated up to 300 °C to eliminate any remaining organic matter. Once ashes were acquired, they were grounded for 30 minutes each to obtain fine powders, and then sintered for 24 hours at 600 °C in air. A second grinding was performed for each powder, and finally they were sintered again for 24 hours at 900 °C in air.

The crystal structure was analyzed using X-ray powder Diffraction (XRD) with an Empyrean PANalytical diffractometer, utilizing a Cu X-ray source ($\lambda = 1.54056$ Å) and Bragg–Bentano geometry (2θ) over a range of 20° to 90° with a step size of 0.019 in 2θ. Magnetic properties were measured employing a SQUID magnetometer (MPMS XL7, Quantum Design) within a temperature range of 100–300 K and magnetic fields up to 7 T. The magnetocaloric effect, representing magnetic entropy change, was determined from the magnetic isotherms for all examined compounds.

3 Results and discussion

3.1 Structural characterization

The experimental XRD data analyzed through Rietveld refinement using the FULLPROF software[17] and fitted with Pseudo-Voigt function indicate that all three samples are single-phase materials, and exhibit a rhombohedral perovskite structure with the $R\bar{3}C$ space group[16,18] as shown in Fig. 1a–c.

Fig. 1d–f illustrate that the splitting of the main peak becomes more pronounced for sample LS3, and this type of splitting is indicative of the rhombohedral distortion in the lattice. In addition, the crystal structure of the samples appears to be weakly influenced by the gel formation temperature during the synthesis process, as the peaks are obtained nearly at the same diffraction angle (2θ) for all samples. Furthermore, a lower gelation temperature is associated with a more stable crystalline structure.

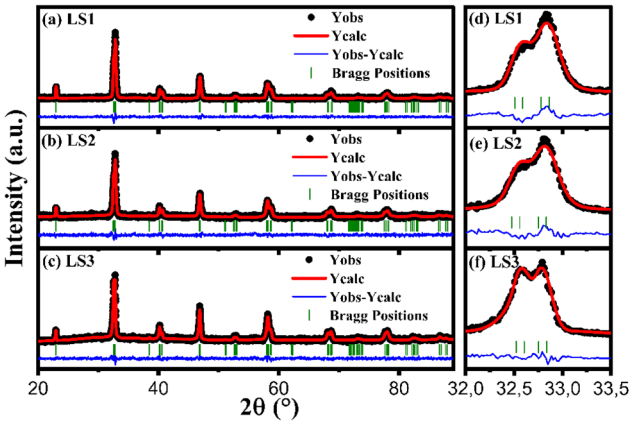

Fig. 1 Calculated XRD spectra of LS1 (a), LS2 (b) and LS3 (c) after Rietveld refinement. Zoom on the main peak of LS1 (d), LS2 (e) and LS3 (f).

The determined lattice parameters obtained from the refinements are presented in Table 1 and depicted in Fig. 1.

Table 1 Lattice parameters, crystallite size, manganese–oxygen bond length, and manganese–oxygen angles for LS1, LS2 and LS3 samples

Sample	LS1	LS2	LS3
Space group	$R\bar{3}C$	$R\bar{3}C$	$R\bar{3}C$
Lattice parameters			
$a = b$ (Å)	5.5043	5.5095	5.5017
c (Å)	13.3202	13.3319	13.3387
V (Å^3)	349.5089	350.4720	349.6561
$\theta_{Mn-O-Mn}$	162.1438	163.2758	162.2403
d_{Mn-O}	1.96207	1.96092	1.96207
Atomic positions			
La/Sr x	0	0	0
La/Sr y	0	0	0
La/Sr z	0.25	0.25	0.25
Mn/Co x	0	0	0
Mn/Co y	0	0	0
Mn/Co z	0	0	0
O x	0.44468	0.44824	0.44495
O y	0	0	0
O z	0.25	0.25	0.25
Agreement factors			
R_{exp} (%)	8.58	9.50	8.60
R_{wp} (%)	9.68	8.95	9.72
R_p (%)	7.46	7.11	7.53
χ^2	1.447	1.762	1.415
Cristallite sizes			
D_{Sc} (nm)	30.369	26.478	39.583
D_{W-H} (nm)	84.733	34.394	73.369
Strain	1.64×10^{-3}	1.07×10^{-3}	1.44×10^{-3}

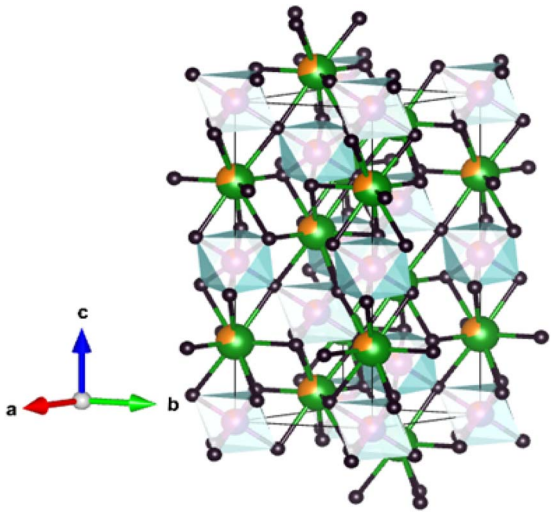

Fig. 2 Unit cell of LS1 obtained by Vesta software: La (in green), Sr (in orange), octahedral site: Mn (in purple), Co (in red) and O (in black).

The unit cell representation, generated using Vesta software, showcases the atomic positions within the crystal lattice. Fig. 2 demonstrates the unit cell representation for one sample, LS1, as all three samples share the identical unit cell structure.

The calculated crystallite sizes using Scherrer formula,[19] denoted as D_{Sc}, are presented in Table 1. The formula links the crystallite size to the peak broadening β, wavelength λ of the X-ray radiation, and the scattering angle θ using eqn (1), where K equals 0.9:

$$D_{Sc} = \frac{\lambda K}{\beta \cos(\theta)} \quad (1)$$

Additionally, crystallite sizes were carried out using the Williamson–Hall plot method,[20] as shown in Table 1, utilizing eqn (2):

$$\beta \cos(\theta) = \frac{K\lambda}{D_{W-H}} + 4\varepsilon \sin(\theta) \quad (2)$$

Here D_{W-H} denotes the crystallite size, and ε denotes the internal strain.

Fig. 3 illustrates representative Williamson–Hall plots for LS1, LS2 and LS3 compounds. Measurements by Scherrer method vary between 26.478 nm to 39.583 nm, while the Williamson–Hall method indicates sizes from 34.394 nm to 84.733 nm (see Table 1). These variations are likely to be due to different growth conditions, particularly gelation temperatures. The obtained strain values imply that distortions are minimized and that the samples have a well-ordered crystal structure with a minimum of imperfections. They also decrease as the crystallite sizes decrease.

3.2 Magnetic properties

3.2.1 Measurement of magnetization as a function of temperature. Fig. 4a–c confirm the phase transition in all three samples from a ferromagnetic state at low temperatures to a paramagnetic state at higher temperatures, in accordance with the principle of electrical neutrality. Since the compound $La_{0.8}^{3+}Sr_{0,2}^{2+}Mn_{0.6}^{3+}Mn_{0.2}^{4+}Co_{0.2}^{3+}O_3^{2-}$ is composed of (0.6) Mn^{3+} ions and (0.2) Mn^{4+} ions per formula unit, the Mn^{3+}/Mn^{4+}

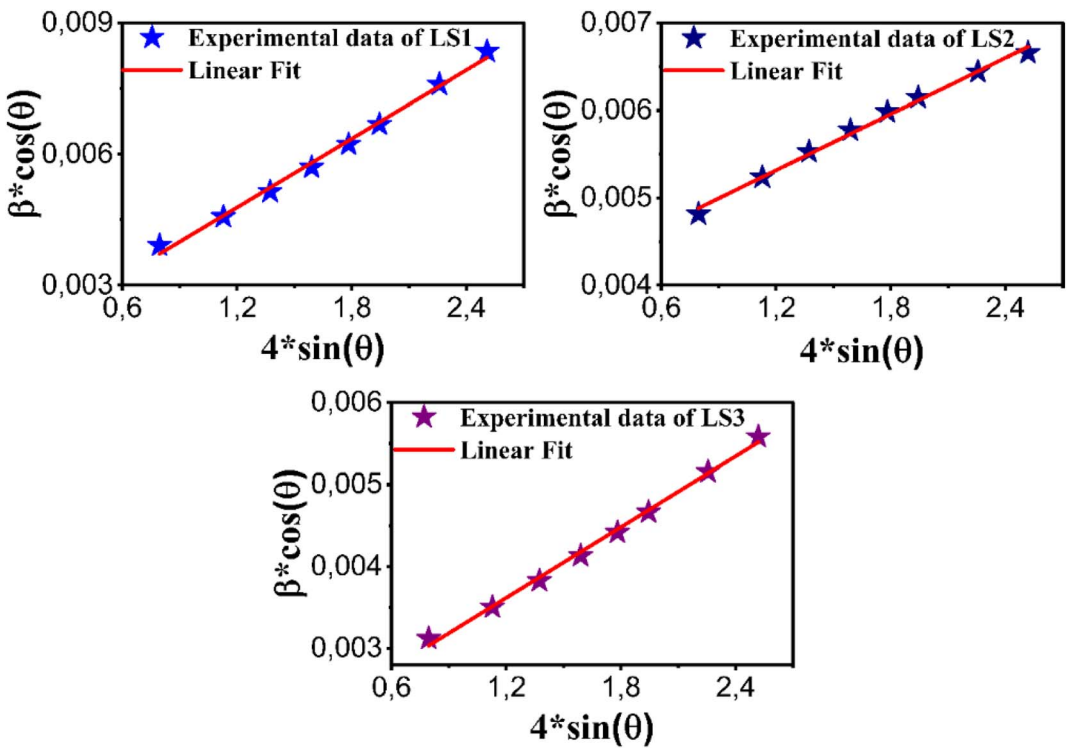

Fig. 3 Graphical representation of the Williamson–Hall method for LS1, LS2 and LS3 samples.

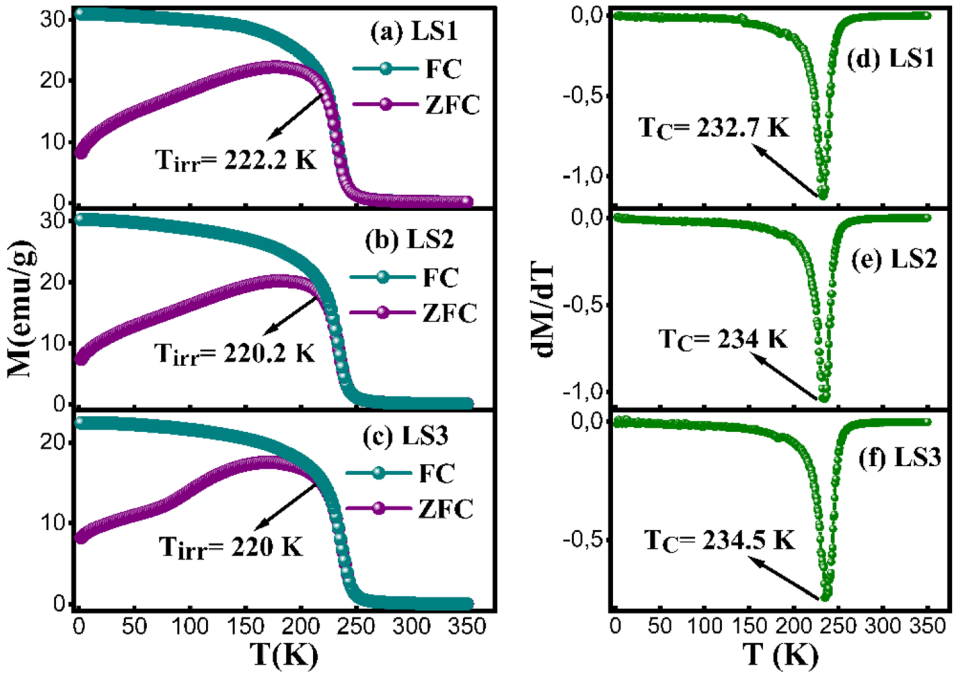

Fig. 4 Temperature dependence of zero-cooled-field (ZFC) and field cooled (FC) magnetization under 500 Oe of LS1 (a), LS2 (b), LS3 (c). Determination of Curie temperature of LS1 (d), LS2 (e), LS3 (f).

ratio of 3 in the compound fosters the occurrence of double exchange interactions, leading to the manifestation of ferromagnetic behavior at low temperatures.

The magnetization behavior of LS1, LS2 and LS3 samples was examined under a 500 Oe magnetic field during both zero-field cooling (ZFC) and field-cooling (FC) processes. The $M_{ZFC}(T)$ curves illustrate a rise in magnetization as temperature increases, reaching its peak at 178.2 K for LS1, 182.2 K for LS2 and 172.2 K for LS3. This behavior can be attributed to the presence of both ferromagnetic (FM) and antiferromagnetic (AFM) clusters or magnetic inhomogeneity.[21] The decrease observed in the ZFC curve of LS3 sample near $T = 100$ K can be attributed to the presence of short range antiferromagnetic clusters,[22] probably due to a high gelation temperature during the synthesis process. These clusters induce local variation in the magnetic interactions that affect the magnetic response of the compound.

Above these temperatures, the magnetization exhibits a rapid decline due to the ferromagnetic-paramagnetic phase transition, which leads to the disordering of magnetic moments influenced by thermal energy.

When the temperature drops to 222.2 K for LS1, 220.2 K for LS2 and 220 K for LS3, the ZFC and FC magnetization curves begin to separate. Upon surpassing this point at T_{irr}, ΔM the difference between M_{FC} and M_{ZFC}, becomes apparent, providing evidence for the presence of an irreversible transition point.[16]

In comparison to previous research results, where $La_{0.8}Sr_{0.2}Mn_{0.8}Co_{0.2}O_3$ synthesized using the sol–gel method exhibited a Curie temperature T_C of 240 K,[15] LS1, LS2 and LS3 samples yielded slightly lower T_C values.

Fig. 4d–f show the Curie temperatures T_C of the three samples, determined from the minimum of the first derivative curves $dM_{FC}(T)/dT$ as a function of T, which are approximately 232.7 K for LS1, 234 K for LS2 and 234.5 K for LS3. T_C appears to be influenced by gel formation temperature, with an observed increase with increasing temperature. This correlation can be due to certain structural factors.

Fig. 5 illustrates the variation of ΔM as a function of temperature. ΔM values are high in all three samples at temperatures below T_C, indicating that the magnetic field of 500 Oe was not sufficient for aligning the magnetic moments at low temperatures, which resulted in strong magnetic anisotropies in all three samples. In addition, ΔM decreases with gelation temperature increasing, indicating that the magnetic moments in LS3 are more ordered than those in LS1 and LS2.[23]

The real part of susceptibility χ' for all three samples shows similar curves measured at 1 Hz, 10 Hz and 100 Hz frequencies under 500 Oe applied field as shown in Fig. 6a and c, (curves pertaining to LS1 are not shown because they are identical to those of LS2), indicating a negligible dependence of the applied magnetic field. As the applied frequency increases, χ' curves exhibit a slight shift towards higher temperature values, suggesting a frequency-dependent influence on the magnetic ordering. The increase in χ' up to a certain point, named T_f, followed by a gradual decrease implies the presence of magnetic transitions, which may be associated with a paramagnetic-ferromagnetic phase transition.[24]

A second peak is observed in the χ'' *versus* temperature curves at low temperature as depicted in Fig. 6b and d. In order to check whether LS1, LS2 and LS3 exhibit spin-glass behavior, Mydosh parameter $\Omega = \Delta T_f/(T_f \Delta \log(f))$ needs to be calculated, T_f the temperature of the peak in ac susceptibility *versus* temperature also called the freezing temperature and f is the frequency.[25,26] Ω

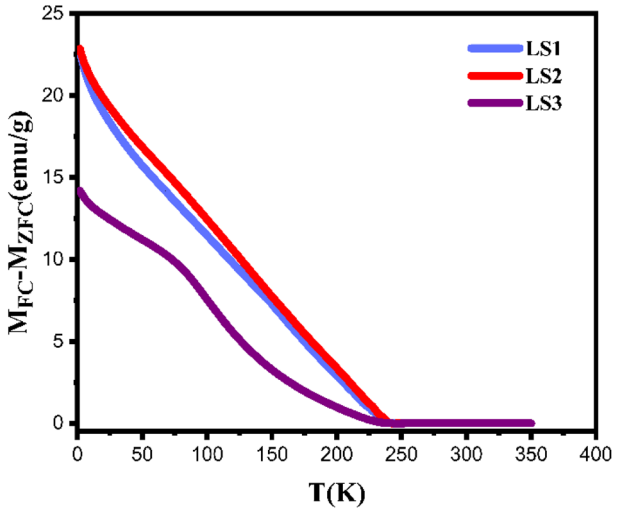

Fig. 5 Temperature dependence of the difference Δ*M* for LS1, LS2 and LS3.

is found to be 0.005 for LS1 and LS2, and 0.006 for LS3. It is common that Ω for spin glass systems varies between 0.004 to 0.018,[27] which is the case for LS1, LS2 and LS3 samples.

To understand the dynamic of magnetic nanoparticles and distinguish between superparamagnetic systems and those displaying a spin glass character, three models are commonly used. For the three models, we denote by: E_a the activation energy, K_B the Boltzmann constant and $\tau = 1/2\pi f$.

The Neel–Brown model for superparamagnetic non-interacting nanoparticles expresses τ as follow:[28]

$$\tau = \tau_0 \exp\left(\frac{E_a}{K_B T_f}\right) \quad (3)$$

According to this model, τ_0 for superparamagnetic systems is in the range of 10^{-9} to 10^{-13} s.[28] As it can be seen in Fig. 7a and d, fitting the experimental data of LS2 and LS3 with eqn (3) gives an extremely small values of τ_0 ($\tau_0 \ll 10^{-13}$ s), indicating that the samples do not exhibit superparamagnetic properties.

The Vogel–Fulcher model is used for interacting nanoparticles according to eqn (4):[29]

$$\tau = \tau_0 \exp\left(\frac{E_a}{K_B(T_f - T_0)}\right) \quad (4)$$

where T_0 is the SG transition temperature, which can take values from zero to T_f.

Fig. 7 b and Fig. 7e show experimental data fitted with eqn (4), where E_a/K_B is equal to 404.2 K and 416.6 K, T_0 is equal to 214.25 K and 215 K and τ_0 is found to be 1.15×10^{-13} s and 2.78×10^{-13} s for LS2 and LS3, respectively.

However, for spin glass systems τ_0 is in the range of 10^{-11} to 10^{-13} s,[30] confirming the spin glass behavior in the samples.

Tholence parameter, δ_{Th}, is derived in order to verify the nature of the spin interaction using the following formula:[29]

$$\delta_{Th} = \frac{T_f - T_0}{T_f} \quad (5)$$

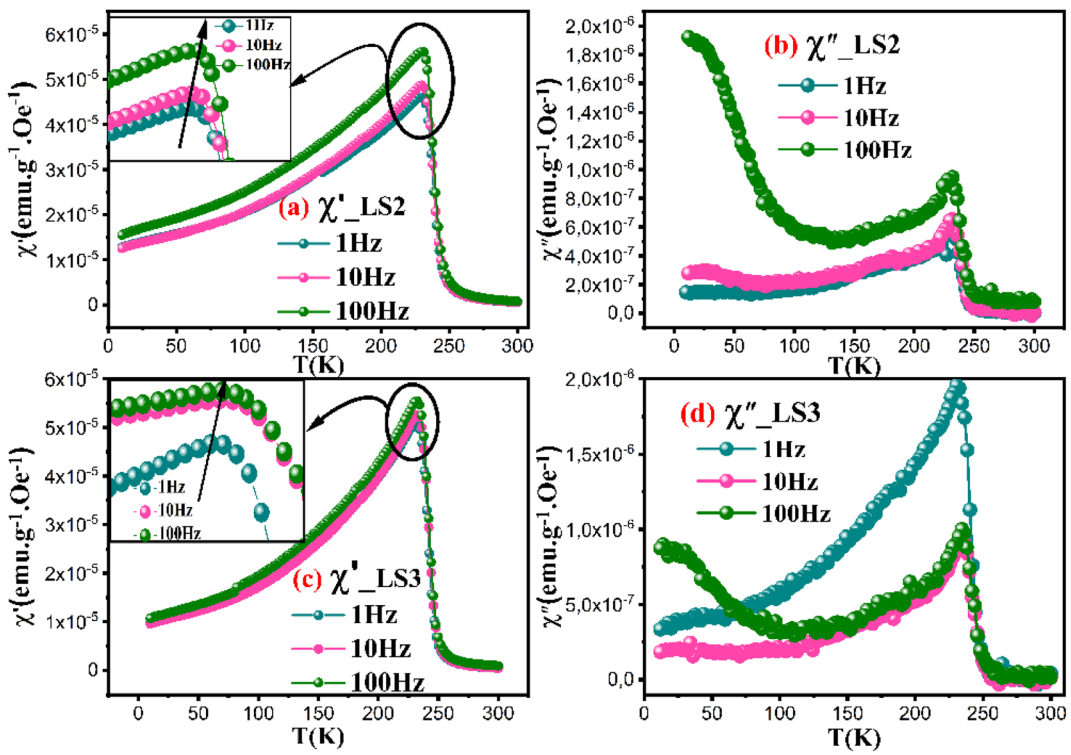

Fig. 6 Variation of real and imaginary parts of AC susceptibility of LS2 and LS3 samples at 1, 10 and 100 Hz under 500 Oe applied magnetic field. Insets: Enlargement of the shift towards high temperatures of the real parts of AC susceptibility of: LS2 (a), LS3 (c).

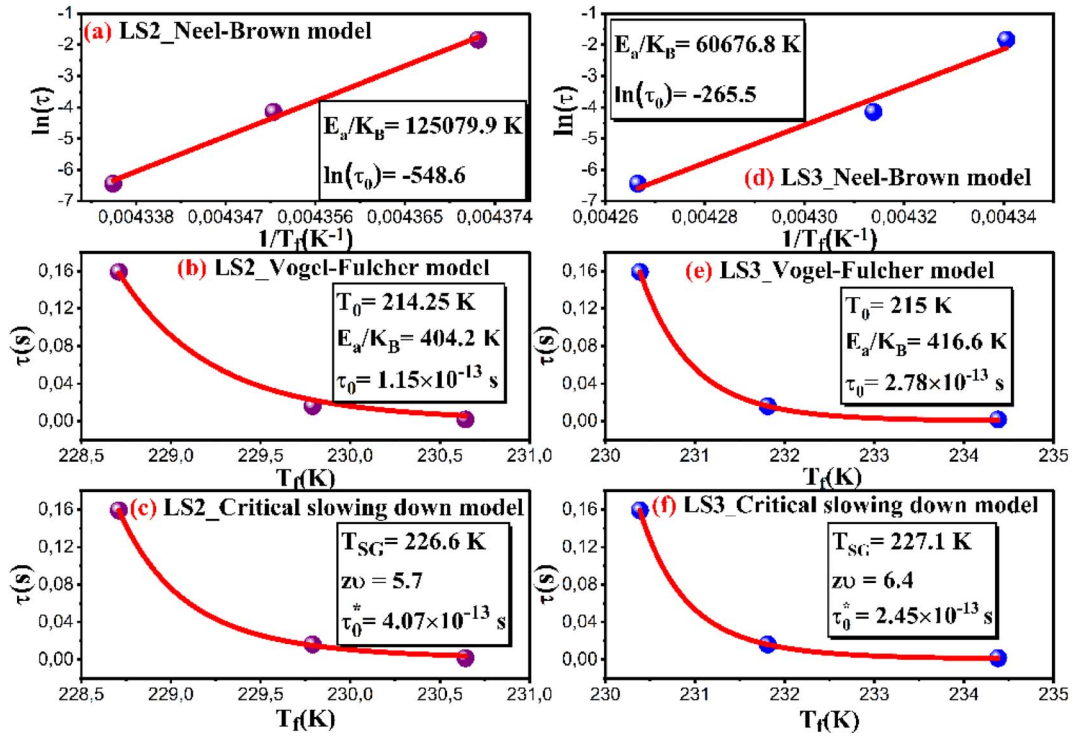

Fig. 7 Appropriate adjustment of AC magnetic susceptibility of samples LS2 and LS3 with: Neel–Brown model (a) and (d), Vogel–Fulcher model (b) and (e), conventional critical slowing down model (c) and (f).

Calculated values of the δ_{Th} parameter using T_0 values obtained from fits with eqn (4) are listed in Table 2. Theoretically, in the medium to strong interaction regime for spin glass system, δ_{Th} ranges between 0.07 and 0.3,[28] which is the case for the samples in this work.

The conventional critical slowing down model is described by the following equation:[29]

$$\tau = \tau_0^* \left(\frac{T_{SG}}{T_f} - 1 \right)^{-z\vartheta} \quad (6)$$

where T_{SG} is the transition temperature, zv is a critical dynamic exponent.

For spin glass systems, zv ranging from 4 to 13 and τ_0^* ranges from 10^{-11} to 10^{-13} s.[31]

From the fitted experimental data with eqn (6) as shown in Fig. 7c and f, τ_0^* is found to be 4.07×10^{-13} s and 2.45×10^{-13} s, zv is found to be 5.7 and 6.4, T_{SG} is found to be 226.6 K and 227.1 K for LS2 and LS3, respectively. These results confirm the spin glass behavior in LS1, LS2 and LS3 samples.

3.2.2 Magnetic characteristics in the paramagnetic phase ($T > T_C$). The examination of magnetic properties in the paramagnetic phase is based on analyzing the change in the inverse magnetic susceptibility with respect to temperature, as shown in Fig. 8.

In the case of a ferromagnetic material beyond the transition, the susceptibility follows the Curie–Weiss law:

$$\chi = \frac{C}{T - \theta\omega} \quad (7)$$

where θ_ω represents the paramagnetic Weiss temperature and C denotes the Curie constant, which is given by:

$$C = \frac{N\mu_{eff}{}^2}{3K_B} \quad (8)$$

where $N = 6.02214076 \times 10^{23}$ mol^{-1}, $K_B = 1.38 \times 10^{-16}$ erg per K and μ_{eff} is the effective magnetic moment estimated from the Curie constant using the formula:

$$\mu_{eff}\ (\mu_B) = \sqrt{\frac{3CK_B}{N}}\mu_B \quad (9)$$

where $\mu_B = 7.96 \times 10^8$ emu.

The theoretical value of the effective moment can be calculated using the general formula:

$$\mu_{eff} = g\sqrt{J(J+1)}\mu_B \quad (10)$$

where $J = L + S$, L represents the total orbital angular momentum, S represents the spin angular momentum, and g is the Landé factor.

For transition metals with nd^x electron configuration, the expression of the effective moment is given as:

Table 2 Calculated δ_{Th} parameter at different frequency values

Frequency	δ_{Th}(LS2)	δ_{Th}(LS3)
1 Hz	0.07	0.072
10 Hz	0.072	0.078
100 Hz	0.076	0.09

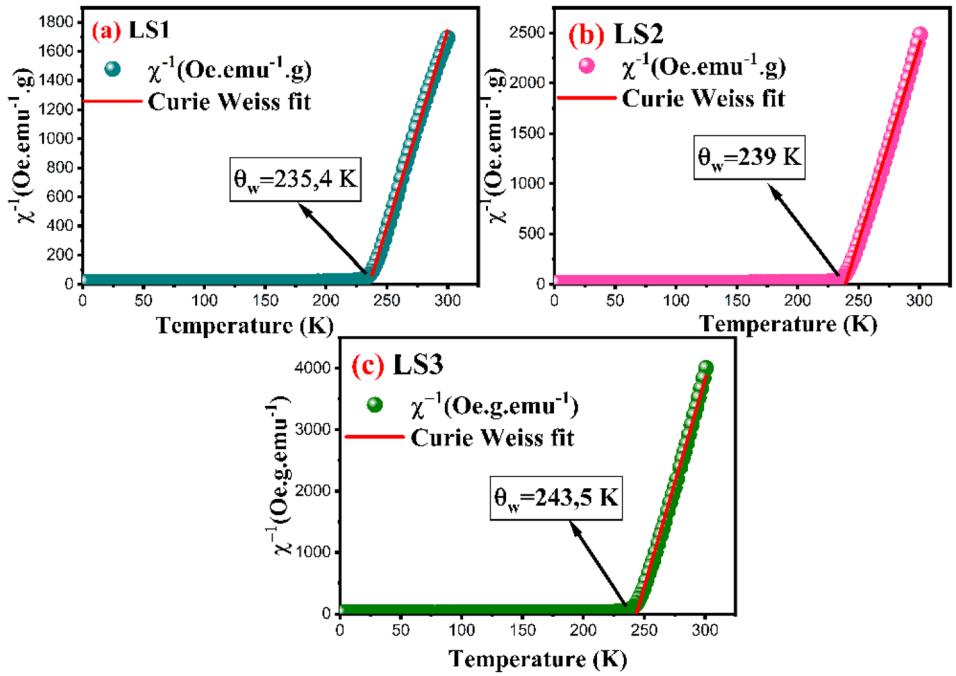

Fig. 8 Inverse susceptibility of LS1, LS2 and LS3 derived from magnetization measurements at 500 Oe.

$$\mu_{\text{eff}} = g\sqrt{S(S+1)}\mu_{\text{B}} \tag{11}$$

Table 3 presents the values of the experimental Curie constant, Weiss temperature, the experimental and theoretical effective moments of LS1, LS2 and LS3 samples.

$$\mu_{\text{eff}} = \sqrt{n_{\text{Mn}^{3+}} \times {\mu_{\text{eff}}}^2(\text{Mn}^{3+}) + n_{\text{Mn}^{4+}} \times {\mu_{\text{eff}}}^2(\text{Mn}^{4+}) + n_{\text{Co}^{3+}} \times {\mu_{\text{eff}}}^2(\text{Co}^{3+})} \tag{13}$$

Considering $g = 2$, theoretical effective moments μ_{eff} of $Mn^{3+}(S = 2)$, $Mn^{4+}(S = 3/2)$ and $Co^{3+}(S = 2)$ are respectively $4.9\mu_B$, $3.9\mu_B$ and $4.9\mu_B$. Therefore, the values of the total theoretical effective moments of different compounds can be obtained using the following formula:

$$\mu_{\text{eff}} = \sqrt{\sum_i n_i \left(\mu_{\text{eff}}(i)\right)^2} \tag{12}$$

For LS1, LS2 and LS3 samples, the effective moment is expressed as:

Table 3 Experimental Curie constant, Weiss temperature, experimental and theoretical magnetic moments for LS1, LS2 and LS3 samples

Sample	C (K emu Oe^{-1} mol^{-1})	θ_ω (K)	$\mu_{\text{eff}}^{\text{th}}$ (μ_B)	$\mu_{\text{eff}}^{\text{exp}}$ (μ_B)
LS1	8.596	235.4	4.712	8.293
LS2	5.915	239	4.712	6.879
LS3	3.436	243.5	4.712	5.243

Experimental values of the effective magnetic moments for the three samples, derived from fitting the χ^{-1} as a function of temperature using eqn (7), are consistently higher than the theoretical values, which can be predominantly attributed to the presence of ferromagnetic inhomogeneities within the paramagnetic phase.[32,33]

The hypothesis is supported by the $\theta\omega$ values, which exceed the Curie temperature for each sample.

3.2.3 Hysteresis curves. Hysteresis curves shown in Fig. 9 illustrate the ferromagnetic behavior of the samples at low temperatures (5 K, 10 K and 100 K).

LS1, LS2 and LS3 samples require a relatively high magnetic field for attaining saturation magnetization. In this case, hysteresis curves can be fitted in order to quantify saturation, remanence and coercivity at low temperatures using the following equation:[34]

$$M(H) = 2\frac{M_s}{\pi}\,\text{artan}\left[\left(\frac{H \pm H_c}{H_c}\right)\tan\left(\frac{\pi}{2}\frac{M_r}{M_s}\right)\right] + \chi H \tag{14}$$

Furthermore, the utilization of this equation for fitting enables the determination of the magnetic susceptibility values, along with the relative fractions of ferromagnetic and

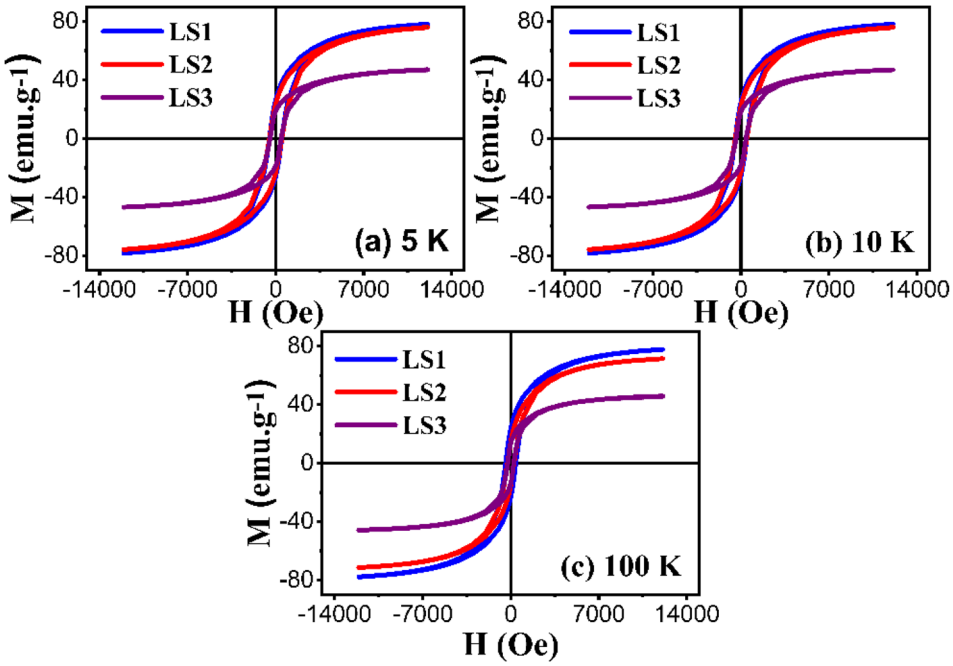

Fig. 9 Hysteresis curves at 5 K (a), 10 K (b) and 100 K (c) of LS1, LS2 and LS3 samples.

antiferromagnetic contributions that are present in the LS1, LS2 and LS3 samples. Fig. 10 displays an example of hysteresis curves (at 5 K) that have been fitted with eqn (14).

Table 4 shows the results of the analysis of the low temperature hysteresis carried out at 5, 10 and 100 K using eqn (14). The low coercivity observed indicates that the samples have a soft ferromagnetic nature. The hysteresis cycle areas are also significantly reduced, suggesting lower energy losses during the cycle, which is important for the magnetic refrigeration. In addition, the ferromagnetic behavior dominates in the samples, as indicated by the higher percentages of ferromagnetic contribution compared to the antiferromagnetic contribution.

To study the effect of magnetic anisotropy on the properties of the samples and to determine the anisotropy parameters (the anisotropy constant K and the anisotropy field H_a), it is required

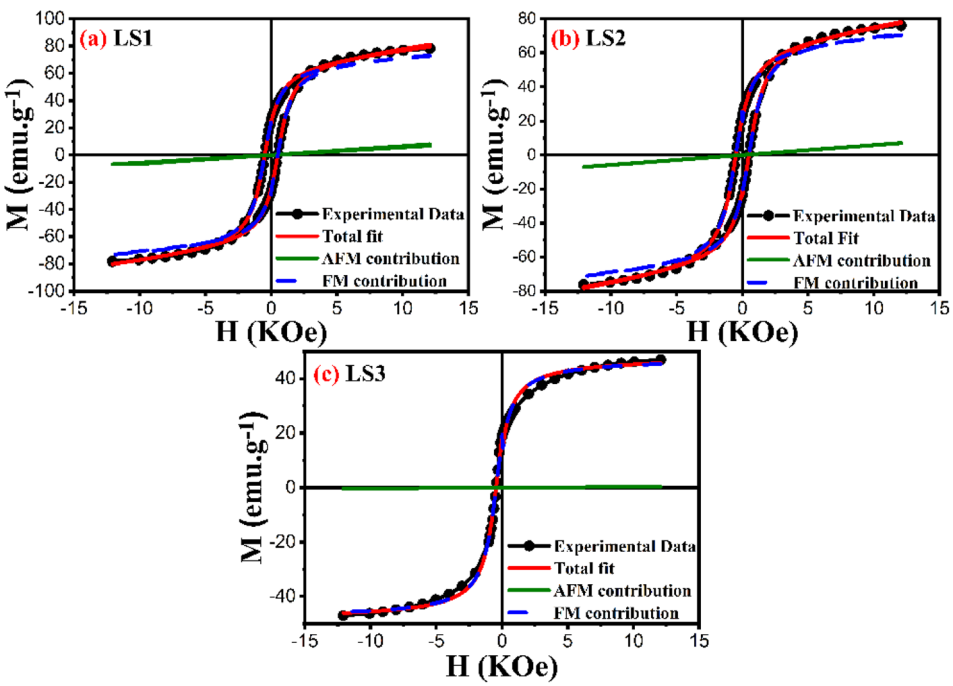

Fig. 10 Hysteresis curves at 5 K of LS1 (a), LS2 (b) and LS3 (c) fitted with eqn (14).

Table 4 Anisotropy and magnetic properties obtained from fitting the hysteresis curves at low temperatures (5 K, 10 K and 100 K) for LS1, LS2 and LS3 samples

Temperature	5 K			10 K			100 K		
Sample	LS1	LS2	LS3	LS1	LS2	LS3	LS1	LS2	LS3
a (Oe)	1114.05	1190.71	1062.06	703.79	648.94	241.91	794.09	772.33	769.37
b (Oe^2)	832 700.21	909 909.93	836 376.03	286 112.41	232 981.23	32 988.33	339 048.38	303 133.11	358 969.05
k (erg cm^3)	120 922.33	105 419.93	121 188.93	71 885.86	62 560.03	13 129.59	75 344.74	69 216.69	45 376.60
H_a (Oe)	3534.19	3694.41	3541.98	2071.64	1869.42	679.58	2255.16	2132.37	2320.46
χ (emu g^{-1} Oe^{-1})	5.65×10^{-4}	5.79×10^{-4}	2.87×10^{-5}	6.02×10^{-4}	5.78×10^{-4}	4.53×10^{-4}	4.67×10^{-4}	4.52×10^{-4}	3.66×10^{-4}
H_c (Oe)	511.93	482.01	466.08	477.14	477.54	426.58	253.23	260.53	242.85
M_{FM}^s (emu g^{-1})	68.43	57.07	47.17	66.93	66.93	38.64	66.82	64.92	39.11
M_{FM}^r (emu g^{-1})	24.81	18.88	15.53	23.73	20.97	16.64	14.17	12.52	11.03
% FM	91.42	90.86	99.24	99.94	99.94	99.99	99.95	99.95	99.96
% AFM	8.58	9.14	0.76	9.11	0.06	0.01	0.05	0.05	0.04

to adjust the hysteresis curves to higher fields ($H \gg H_C$) using the law of approach to saturation,[35] defined by eqn (15):

$$M = M_s\left(1 - \frac{a}{H} - \frac{b}{H^2}\right) + \chi H \quad (15)$$

Here M_s is the saturation magnetization, $\frac{a}{H}$ represents the contributions of inclusions/microstress, $\frac{b}{H}$ represents the contribution of magnetocrystalline anisotropy and χH is the forced magnetization term.

The constant b for a cubic system is related to the anisotropy constant K and to the magnetization of saturation M_s by the following equation:

$$K = M_s\sqrt{\frac{15b}{4}} \quad (16)$$

where the anisotropy constant K is related to the anisotropy field H_a by the expression below:

$$H_a = \frac{2K}{M_s} \quad (17)$$

As shown in Table 4, for each of the samples, the K value is higher at 5 K (of the order of 10^5 erg cm^3) than at 10 and 100 K, indicating that the samples are more magnetically ordered at 5 K than at 10 and 100 K. Also, at 10 and 100 k, the values of the anisotropy constant decrease with increasing gelation temperature, whereas at 5 K the anisotropy values are approximately the same for all three samples.

At ambient temperature ($T = 300$ K), the hysteresis curves for LS1, LS2 and LS3 exhibit clear paramagnetic behavior. This observation is supported by the positive susceptibility values, which are expected to be in the range of 10^{-3} to 10^{-5} for all three samples. The determination of χ can be graphically obtained from the slope of *M versus H* curves as it is presented in Fig. 11. The χ values are respectively 4.3×10^{-4} emu g^{-1} Oe^{-1} for LS1, 3.7×10^{-4} emu g^{-1} Oe^{-1} for LS2 and 2.6×10^{-4} emu g^{-1} Oe^{-1} for LS3.

The hysteresis curve of sample LS1 exhibits a slight deviation, as illustrated in Fig. 11, which could potentially be attributed to the presence of ferromagnetic clusters.

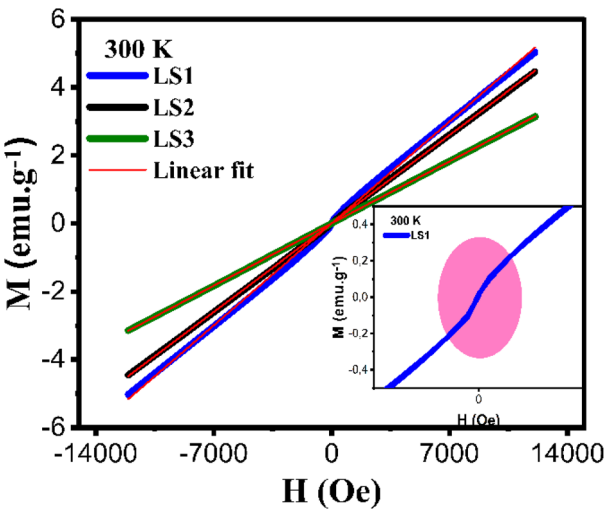

Fig. 11 Hysteresis curves at 300 K of LS1, LS2 and LS3. Inset: Enlargement of the hysteresis deviation region of the sample LS1.

3.2.4 Measurements of magnetization as a function of applied magnetic field. Fig. 12 demonstrates a progressive transition, for all the samples, from a ferromagnetic state to a paramagnetic state as the temperature rises. This is supported by the almost linear M–H curves observed for each sample at high temperatures. Furthermore, the saturation magnetization of each sample decreases as the gel formation temperature decreases owing to the diminishing in double exchange interactions with raising temperature.[15]

The M–H isothermal curves of the three samples did not display any S-shaped magnetization indicating that all samples exhibited a second-order magnetic transition.[16,36] To confirm this supposition, Arrot plots were generated[37] as shown in Fig. 13.

The Arrot plots of the three samples did not exhibit a series of parallel lines, as expected for long-range ferromagnetic order. Instead, they showed nonlinearity suggesting the presence of short-range magnetic order.

The curves in both temperature regions, $T < T_C$ and $T > T_C$, for low values of H/M are set in converse orientations, confirming the ferromagnetic-paramagnetic transition.[14]

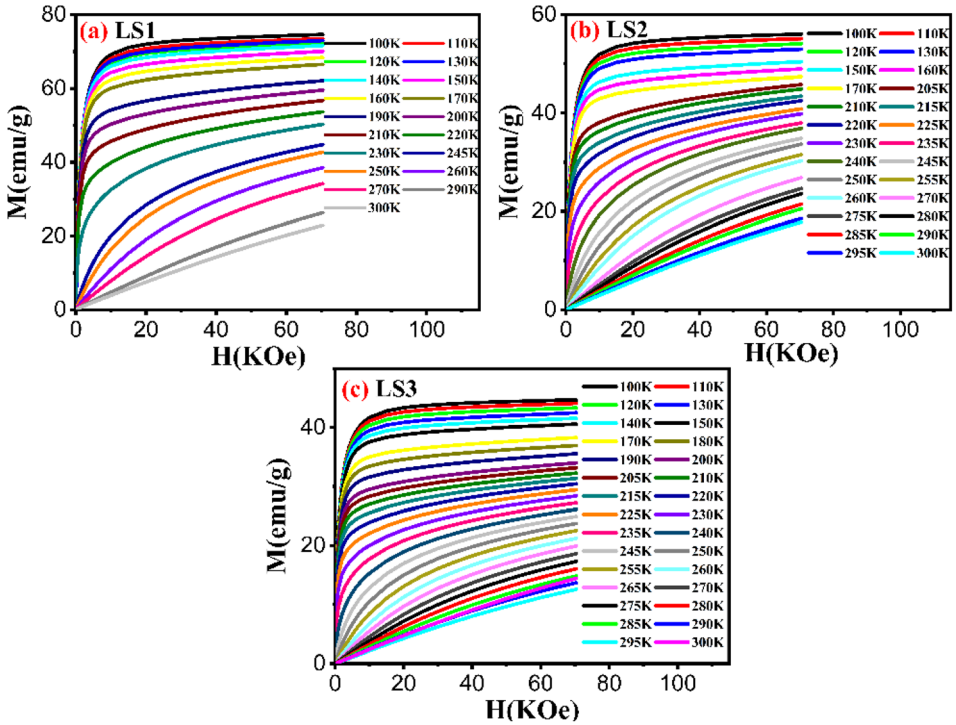

Fig. 12 Variation of magnetization as a function of applied magnetic field of LS1 (a), LS2 (b) and LS3 (c) samples.

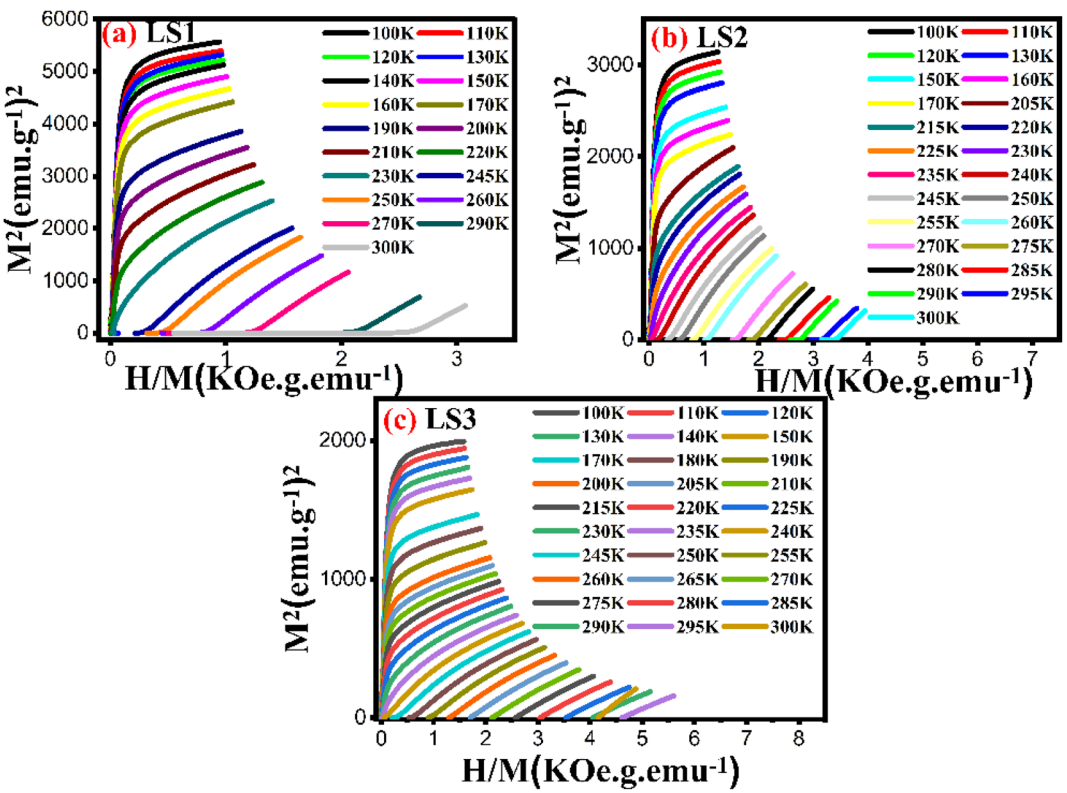

Fig. 13 Arrot plots analysis of LS1 (a), LS2 (b) and LS3 (c) samples.

The nature of the magnetic transition was verified using Banjeree criterion. The slopes of the Arrot plots generated for LS1, LS2, and LS3 remained positive over the entire temperature range measured near T_C, indicating the presence of a second order-phase transition for each sample, as determined by the Banjeree criterion.[38]

3.3 Magnetocaloric effect

Although magnetometers are primarily designed to measure the total magnetization M directly, the entropy change can be calculated from the isothermal magnetization $M(H)_T$ or the isofield magnetization $M(T)_H$ using the Maxwell relation:[39]

$$\Delta S\ (T,\ \Delta H = H_f - H_i) = \mu_0 \int_{H_i}^{H_f} \left(\frac{\partial M}{\partial T}\right)_H dH \qquad (18)$$

Fig. 14 depicts the variation of magnetic entropy change ΔS as a function of temperature for LS1, LS2 and LS3 at different magnetic field values $H = 0.5$, 1, 1.5, 2, 3, 4, 5, 6 and 7 T.

The temperature dependent behavior of $(-\Delta S)$ shows an initial rise until reaching a certain point around the Curie temperature, followed by a gradual decline. This along with the observed increase in $(-\Delta S)$ with higher magnetic field values, suggests that the samples are good candidates for application such as magnetic refrigeration.

Table 5 and Fig. 14 show that the sample formed at the lower gelation temperature, LS1, has the highest $(-\Delta S)$ value for each value of the applied magnetic fields, indicating that the gel formation temperature has a significant influence on the magnetic properties of the samples.

Also, $|-\Delta S_{max}|$ for LS1 and LS2 (3.24 and 2.89 J kg^{-1} K^{-1} respectively) under applied magnetic field of 5 T remains greater than $|-\Delta S_{max}|$ of $La_{0.8}Sr_{0.2}Mn_{0.8}Co_{0.2}O_3$ (2.36 J kg^{-1} K^{-1})[16] under an applied magnetic field of 7 T. This result reveals the influence of the process of synthesis on the magnetic

Table 5 Comparison of the obtained results from the temperature dependent $(-\Delta S)$ curve variations for LS1, LS2 and LS3 samples with reported results of the Gd magnetic refrigerant and other perovskite materials

Sample	H (T)	$\lvert-\Delta S_{max}\rvert$ (J kg^{-1} K^{-1})	RCP (J kg^{-1})	Ref.
Gd	2	5	196	40
Gd	5	10.2	410	41
$La_{0.67}Sr_{0.33}MnO_3$	5	1.69	211	42
$La_{0.84}Sr_{0.16}MnO_3$	5	5.85	240	43
$La_{0.87}Sr_{0.13}MnO_3$	5	5.80	232	43
$La_{0.845}Sr_{0.155}Mn_{0.98}Co_{0.02}O_3$	1.35	2.25	52	44
$La_{0.67}Sr_{0.33}Mn_{0.9}Co_{0.1}O_3$	5	3.1	156	45
$La_{0.8}Sr_{0.2}Mn_{0.8}Co_{0.2}O_3$	7	2.36	—	16
LS1	2	1.66	78.41	This work
	5	3.25	209.83	
LS2	2	1.45	75.06	This work
	5	2.89	191.09	
LS3	2	1.02	43.54	This work
	5	1.95	110.83	

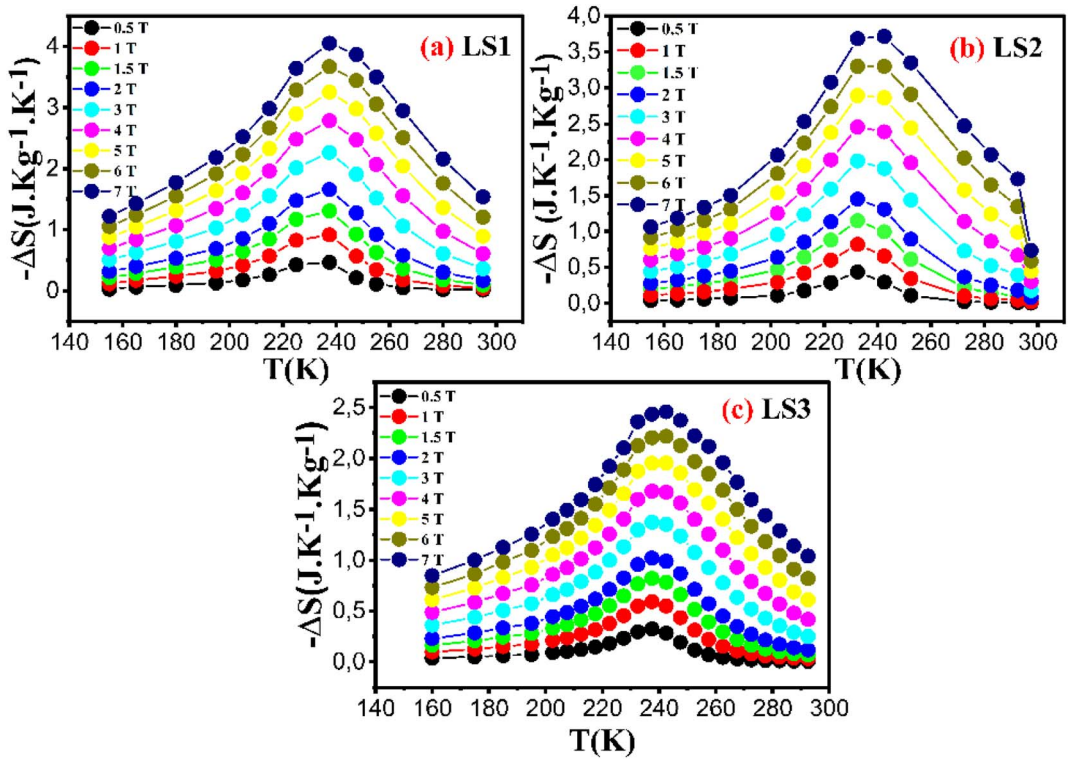

Fig. 14 Variation of magnetic entropy change of LS1 (a), LS2 (b) and LS3 (c) as a function of temperature at different magnetic field values ranging from 0.5 T to 7 T.

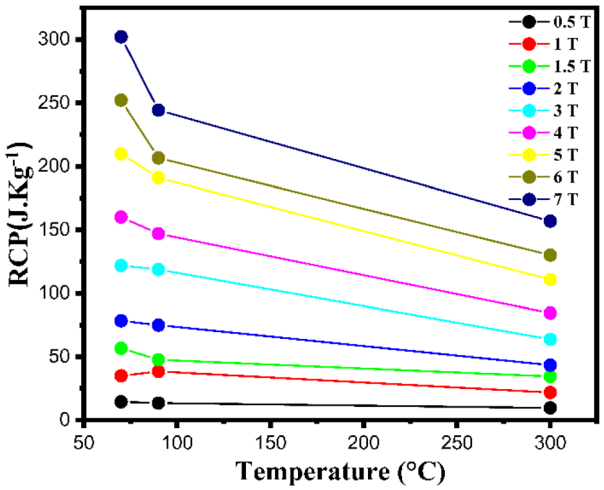

Fig. 15 Variation of RCP coefficient as a function of gelation temperature of LS1, LS2 and LS3 samples at different magnetic field ranging from 0.5 T to 7 T.

properties of the samples and suggests that LS1 and LS2 could be the best performers in the field of magnetic cooling.

The relative cooling power RCP, also known as the cooling coefficient of performance, can be determined by multiplying the maximum magnetic entropy change by the full width at half-maximum δT_{FWHM} of the $\Delta S_{max}(T, H)$ curve following the expression below:[41]

$$RCP = -\Delta S_{max} \partial T_{FWHM} \quad (19)$$

Table 5 presents The RCP values, and Fig. 15 illustrates the variation of RCP coefficient of the three samples as a function of gelation temperature. The results indicate that the sample LS1, with a lower gelation temperature, shows higher RCP values (~210 J kg^{-1} for LS1, 191 J kg^{-1} for LS2, and 111 Jkg^{-1} for LS3 under 5 T).

In addition, as shown in Table 5, the RCP values for LS1, which are approximately 50% of those for pure Gd, position our compounds as promising candidates for potential use in magnetic refrigeration applications.

For a better evaluation of magnetocaloric materials for solid state cooling applications, the study of temperature average entropy change (TEC) is required. Unlike traditional measures such as ΔS and RCP, the TEC parameter is proposed as a more suitable metric to determine the performance of a magneto-caloric material and to provide a more comprehensive analysis by considering entropy changes over a range of temperatures.

This parameter can be readily determined from the obtained ΔS (T, H) curves using the following equation:[46]

$$TEC(\Delta T_{H-C}) = \frac{1}{\Delta T_{H-C}} \max \int_{T_{mid}-}^{T_{mid}+} \frac{\Delta T_{H-C}}{2} |\Delta S(T)| dt \quad (20)$$

where ΔT_{H-C} is a specific temperature range defined by the difference between the hot temperature (T_H) and the cold temperature (T_C) of the reservoirs. T_{mid} refers to the average midpoint maximizing the integral. In our study, ΔH was set at 2 T and 5 T and ΔT_{H-C} was fixed between 10 and 50 K with a step of 5 K.

Fig. 16a and b show the dependence of the TEC parameter on ΔT_{H-C} for LS1, LS2 and LS3 samples at 2 T and 5 T respectively.

As can be clearly seen from Fig. 16, the TEC values decrease with increasing gel formation temperature and increase with increasing ΔH. They are maximal for the LS1 compound, especially for $\Delta H = 5$ T and $\Delta T_{H-C} = 10$ K, where TEC ~3.2 J kg^{-1} K^{-1}, making them candidates for magnetocaloric refrigeration.

Furthermore, as ΔT_{H-C} increases, the TEC values decrease for all three samples at 2 T and 5 T. this behavior is observed in other manganite compounds.[47,48]

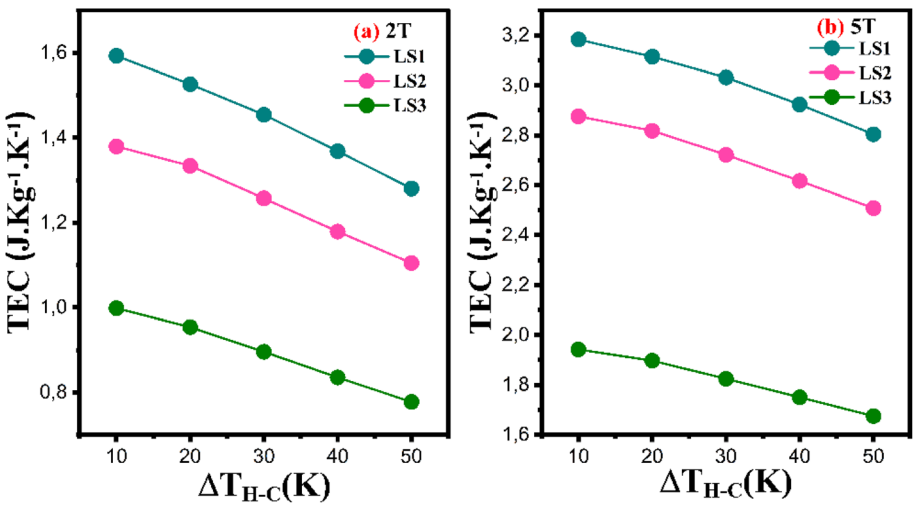

Fig. 16 The temperature average entropy change (TEC) as a function of ΔT_{H-C} for LS1, LS2 and LS3 samples calculated for $\Delta H = 2$ T (a) and $\Delta H = 5$ T (b).

4 Conclusion

The sol–gel synthesis method was successfully applied to the preparation of $La_{0.8}Sr_{0.2}Mn_{0.8}Co_{0.2}O_3$ (LS1, LS2 and LS3) samples with a rhombohedral perovskite structure. In particular, lower gelation temperature were found to improve the structural stability of the samples.

The dynamic magnetic response studied by AC magnetic susceptibility reveals that the LS1, LS2 and LS3 samples exhibit spin glass behavior associated with medium to strong interaction between the magnetic nanoparticles of the samples.

In addition, magnetization measurements and hysteresis curves revealed the soft ferromagnetic behavior of the prepared samples, characterized by low coercive fields. Remarkably, the samples showed promising magnetocaloric effects, indicating their potential for applications in magnetic refrigeration. In particular, LS1 synthesized at the lower gelation temperature showed greater magnetocaloric effects. These results demonstrate the essential role of optimizing the gelation temperature in regulating the magnetic properties and cooling performance of the materials.

Conflicts of interest

There are no conflicts to declare.

Acknowledgements

The authors would like to acknowledge the contribution of Anna Bajorek from the A. Chelkowski Institute of Physics, University of Silesia, for conducting the magnetic measurements.

References

1 P. Narwat, R. J. Choudhary and A. Mishra, Investigating magnetic and magneto-transport properties of ferromagnetic (FM) structure and antiferromagnetic/ferromagnetic (AFM/FM) heterostructures, *Physica B*, 2023, **665**, 415048.

2 I. Dhahri, M. Ellouze, T. Mnasri, E. K. Hlil and R. Jotania, Structural, magnetic, magnetocaloric and critical exponents of oxide manganite $La_{0.7}Sr_{0.3}Mn_{0.95}Fe_{0.05}O_3$, *J. Mater. Sci. Mater. Electron.*, 2020, **31**, 12493–12501.

3 K. Sunita and B. Sonali, Synthesis, physical properties, and biomedical applications of magnetic nanoparticles: a review, *Prog. Biomater.*, 2022, **11**, 1–26.

4 H. Chouaibi, B. Rivas-Murias, M. Smari, J. Massoudi, E. Dhahri and V. Salgueiriño, Unraveling the multi-featured magnetic behavior of $Nd_{0.75}Sr_{0.25}CoO_3$ perovskite nanocrystals annealed at different temperatures, *J. Alloys. Comp.*, 2021, **874**, 159870.

5 D. Deeksha, P. Kour, I. Ahmed, S. Sharma, S. K. Sharma, K. Yadav and Y. K. Mishra, Transition metal based perovskite oxides: emerging electrocatalysts for oxygen evolution reaction, *ChemCatChem*, 2023, **15**, e202300040.

6 X. Zhuojia, Z. Zhengguang, H. Bangrong, L. Lilin and M. Zheng, Research Progress of Doped Manganite Materials in Magnetic Refrigeration, *Front. Mater.*, 2021, **8**, 771941.

7 A. M. Tishin and Y. I. Spichkin, *The Magnetocaloric Effect and its Applications*, CRC Press, Boca Raton, FL, 2016.

8 C. Zener, Interaction between the d-Shells in the Transition Metals. II. Ferromagnetic Compounds of Manganese with Perovskite Structure, *Phys. Rev.*, 1951, **82**, 403.

9 U. K. Sinha, B. Das and P. Padhan, Interfacial reconstruction in $La_{0.7}Sr_{0.3}MnO_3$ thin films: giant low-field magnetoresistance, *Nanoscale Adv.*, 2020, **308**, 2792–2799.

10 J. Liu, W. Q. Wang, H. Y. Wu, Y. Tian, F. Z. Cao and J. J. Zhao, Electromagnetic Property of Co-doped $La_{0.8}Sr_{0.2}MnO_3$ Perovskite Manganese Oxides, *J. Inorg. Mater.*, 2018, **33**, 1237–1247.

11 P. Anil Kumar, A. Nag, R. Matheiu, R. Das, S. Ray, P. Nordblad, A. Hossain, D. Cherian, D. Alba Venero, L. DeBeer-Schmitt, O. Karis and D. D. Sarma, Magnetic polarons and spin-glass behavior in insulating $La_{1-x}Sr_xCoO_3$ ($x = 0.125$ and 0.15), *Phys. Rev. Res.*, 2020, **2**, 043344.

12 M. C. Ramírez Camacho, C. F. Sánchez Valdés, M. Curiel, J. L. Sánchez Llamazares, J. M. Siqueiros and O. Raymond Herrera, Superparamagnetic state in $La_{0.7}Sr_{0.3}MnO_3$ thin films obtained by rf-sputtering, *Sci. Rep.*, 2020, **10**, 2568.

13 T. L. Phan, T. D. Thanh and S. C. Yu, Influence of Co doping on the critical behavior of $La_{0.7}Sr_{0.3}Mn_{1-x}Co_xO_3$, *J. Alloys Compd.*, 2014, **615**, S247–S251.

14 T. D. Thanh, D. C. Linh, T. V. Manh, T. A. Ho, T. Phan and S. C. Yu, Coexistence of short- and long-range ferromagnetic order in $La_{0.7}Sr_{0.3}Mn_{1-x}Co_xO_3$ compounds, *J. Appl. Phys.*, 2015, **117**, 17C101.

15 J. Kuo and G. Sheng-Kai, *Chin. Phys. B*, 2009, **18**, 3035.

16 J. Liu, W. Wang, H. Wu, *et al.*, Negative Magnetic Entropy Change and Critical Behavior of Manganite $La_{0.8}Sr_{0.2}Mn_{1-x}Co_xO_3$ ($x = 0$, 0.2), *J. Low Temp. Phys.*, 2019, **195**, 81–95.

17 J. Rodríquez-Carvajal and T. Roisnel, Line Broadening Analysis Using FullProf: Determination of Microstructural Properties, *Mater. Sci. Forum.*, 2004, **443–444**, 123–126.

18 T. A. Salaheldin, A. A. Ghani, A. E. R. T. AboZied, *et al.*, Synthesis, structural, magnetic and magnetocaloric properties of $La_{0.8}Sr_{0.2}MnO_3$ nanoparticles, *J. Therm. Anal. Calorim.*, 2018, **136**, 621–627.

19 P. Scherrer, Bestimmung der Größe und der inneren Struktur von Kolloidteilchen mittels Röntgenstrahlen, Nachrichten von der Gesellschaft der Wissenschaften zu Göttingen, *Math.-Phys. Kl.*, 1918, **2**, 98–100.

20 Y. T. Prabhu, K. V. Rao, V. S. S. Kumar and B. S. Kumari, *World J. Nano Sci. Eng.*, 2014, **4**, 21–28.

21 J. Moradi, M. E. Ghazi, M. H. Ehsani and P. Kameli, Structural and magnetic characterization of $La_{0.8}Sr_{0.2}MnO_3$ nanoparticles prepared via a facile microwave-assisted method, *J. Solid State Chem.*, 2014, **215**, 1–7.

22 C. Shang, Z. Xia, H. Dai, Y. Wang, D. Liu and X. Zhai, Fe doping induced cluster/spin glass state and metamagnetic

transition in phase separated $La_{0.5}Sr_{0.5}Mn_{1-x}Fe_xO_3$, *J. Magn. Magn. Mater.*, 2024, **590**, 171622.
23 H. Thi Anh, N. N. Huyen and P. D. Thang, Influence of Sr Doping on Magnetic and Magnetocaloric Properties of $Nd_{0.6}Sr_{0.4}MnO_3$, *VNU J. Sci. Math. – Phys.*, 2020, **36**, 2588–1124.
24 D. Yang, P. Zhao, S. Huang, T. Yang and D. Huo, Ferrimagnetism, resistivity, and magnetic exchange interactions in double perovskite La_2CrMnO_6, *Results Phys.*, 2019, **12**, 344–348.
25 Y. Su, Z. Chen, Y. Li, D. Deng, S. Cao and J. Zhang, Effect of Bivalent Cation Ca-Doping on Magnetic Properties in Multiferroic $YMnO_3$ Manganites, *J. Supercon. Novel Magn.*, 2010, **23**, 501–506.
26 N. N. Loshkareva, E. V. Mostovshchikova, A. V. Korolyov, S. V. Naumov, B. A. Gizhevskii, N. I. Solin, L. I. Naumova, S. V. Telegin and L. V. Elokhina, Magnetism and infrared magnetotransmission of $Nd_{0.5}Sr_{0.5}MnO_3$ manganite in nanostate, *J. Magn. Magn. Mater.*, 2013, **341**, 49–55.
27 J. A. Mydosh, *Spin Glasses: an Experimental Introduction*, Taylor & Francis, London, 1993.
28 J. L. Dormann, D. Fiorani and E. Tronc, *J. Magn. Magn. Mater.*, 1999, **202**, 251.
29 J. Massoudi, M. Smari, K. Khirouni, E. Dhahri and L. Bessais, *J. Magn. Magn. Mater.*, 2021, **528**, 167806.
30 D. Gangwar and C. Rath, *Phys. Chem. Chem. Phys.*, 2020, **22**, 14236–14245.
31 J. Souletie and J. L. Tholence, *Phys. Rev. B: Condens. Matter Mater. Phys.*, 1985, **32**, 516.
32 H. Terashita and J. J. Neumeier, Bulk magnetic properties of $La_{1-x}Ca_xMnO_3$ ($0 \leqq x \leqq 0.14$): Signatures of local ferromagnetic order, *Phys. Rev. B: Condens. Matter Mater. Phys.*, 2005, **71**, 134402.
33 S. Zemni, A. Gasmi, M. Boudard and M. Oumezzine, Effect of nominal strontium deficiency on the structure and the magnetic properties of $La_{0.6}Sr_{0.4-\delta}MnO_3$ manganese perovskites, *Mater. Sci. Eng. B*, 2007, **144**, 117–122.
34 Y. Marouani, A. Mabrouki, R. Dhahri, E. Dhahri and B. F. O. Costa, Experimental and theoretical studies of structural, magnetic and electronic properties of $Ba_{1-x}Sr_xFe_{12}O_{19}$ ($x = 0, 0.5, 1$) hexaferrites, *Inorg. Chem. Commun.*, 2022, **136**, 109163.
35 B. D. Cullity and C. D. Graham, *Introduction to Magnetic Materials*, 2nd edn, John Wiley and Sons, Hoboken, NJ, 2011.
36 Y. Zhang, H. Wang, Y. Zhang, Y. Ge and S. H. I. Hua, *Phys. B*, 2013, **410**, 1.
37 A. Arrott, Criterion for Ferromagnetism from Observations of Magnetic Isotherms, *Phys. Rev.*, 1957, **108**, 1394.
38 B. K. Banerjee, On a generalised approach to first and second order magnetic transitions, *Phy. Lett.*, 1964, **12**, 16–17.
39 M. H. Phan and S. C. Yu, Review of the magnetocaloric effect in manganite materials, *J. Magn. Magn. Mater.*, 2007, **308**, 325–340.
40 V. K. Pecharsky and K. A. Gschneidner Jr, Giant Magnetocaloric Effect in $Gd_5(Si_2Ge_2)$, *Phys. Rev. Lett.*, 1997, **78**, 4494.
41 K. A. Gschneidner Jr, V. K. Pecharsky and A. O. Tsokol, Recent developments in magnetocaloric materials, *Rep. Prog. Phys.*, 2005, **68**, 1479.
42 D. T. Morelli, A. M. Mance, J. V. Mantese and A. L. Micheli, Magnetocaloric properties of doped lanthanum manganite films, *J. Appl. Phys.*, 1996, **79**, 373–375.
43 A. Szewczyk, H. Szymczak, A. Wiśniewski, K. Piotrowski, R. Kartaszyński, B. Dabrowski, S. Koleśnik and Z. Bukowski, Magnetocaloric effect in $La_{1-x}Sr_xMnO_3$ for x=0.13 and 0.16, Appl, *Phys. Lett.*, 2000, **77**, 1026–1028.
44 N. Chau, H. N. Nhat, N. H. Luong, D. Le Minh, N. D. Tho and N. N. Chau, Structure, magnetic, magnetocaloric and magnetoresistance properties of $La_{1-x}Pb_xMnO_3$ perovskite, *Physica B: Cond. Matter.*, 2003, **327**, 270–278.
45 C. P. Reshmi, S. Savitha Pillai, M. Vasundhara, G. R. Raji and K. G. Suresh, ManojRaamaVarma, Co-existence of magnetocaloric effect and magnetoresistance in Co substituted $La_{0.67}Sr_{0.33}MnO_3$ at room temperature, *J. Appl. Phys.*, 2013, **114**, 033904.
46 V. Ya. Mitrofanov, S. Kh. Estemirova and G. A. Kozhinaa, Effect of oxygen content on structural, magnetic and magnetocaloric properties of $(La_{0.7}Pr_{0.3})_{0.8}Sr_{0.2}Mn_{0.9}Co_{0.1}O_{3\pm\delta}$, *J. Magn. Magn. Mater.*, 2019, **476**, 199–206.
47 Z. Juan, L. Lirong and W. Gui, Synthesis and magnetocaloric properties of $La_{0.85}K_{0.15}MnO_3$ nanoparticles, *Adv. Powder Technol.*, 2011, **22**, 68.
48 S. Choura-Maatar, M. Nofal Muaffaq, R. M'nassri, W. Cheikhrouhou-Koubaa, N. Chniba-Boudjada and A. Cheikhrouhou, Enhancement of the magnetic and magnetocaloric properties by Na substitution for Ca of $La_{0.8}Ca_{0.2}MnO_3$ manganite prepared via the Pechini-type sol–gel process, *J. Mater. Sci.: Mater. Electron.*, 2020, **31**, 1634–1645.